RESEARCH ARTICLE

**CARBON ENERGY** WILEY

# Thick free-standing electrode based on carbon–carbon nitride microspheres with large mesopores for high-energy-density lithium–sulfur batteries

Hui-Ju Kang[1]  |  Tae-Gyu Lee[1]  |  Heejin Kim[2]  |  Jae-Woo Park[1]  |
Hyun Jin Hwang[3]  |  Hyeonseok Hwang[4]  |  Kwang-Suk Jang[4]  |
Hae Jin Kim[2]  |  Yun Suk Huh[5]  |  Won Bin Im[6]  |  Young-Si Jun[1,3]

[1]Department of Advanced Chemicals & Engineering, Chonnam National University, Buk-gu, Gwangju, Republic of Korea

[2]Division of Analytical Science, Korea Basic Science Institute (KBSI), Yuseong-gu, Daejeon, Republic of Korea

[3]School of Chemical Engineering, Chonnam National University, Buk-gu, Gwangju, Republic of Korea

[4]Department of Applied Chemistry, Hanyang University, Ansan, Gyeonggi-do, Republic of Korea

[5]Department of Biological Engineering, Inha University, Nam-gu, Incheon, Republic of Korea

[6]Division of Materials Science and Engineering, Hanyang University, Seongdong-gu, Seoul, Republic of Korea

**Correspondence**
Kwang-Suk Jang, Department of Applied Chemistry, Hanyang University, 55 Hanyangdeahak-ro, Sangnok-gu, Ansan, Gyeonggi-do 15588, Republic of Korea.
Email: kjang@hanyang.ac.kr

Won Bin Im, Division of Materials Science and Engineering, Hanyang University, 222 Wangsimni-ro, Seongdong-gu, Seoul 04763, Republic of Korea.
Email: imwonbin@hanyang.ac.kr

Young-Si Jun, School of Chemical Engineering, Chonnam National University, 77 Yongbong-ro, Buk-gu, Gwangju 61186, Republic of Korea.
Email: ysjun@jnu.ac.kr

**Abstract**

The development of sulfur cathodes with high areal capacity and high energy density is crucial for the practical application of lithium–sulfur batteries (LSBs). LSBs can be built by employing (ultra) high-loading sulfur cathodes, which have rarely been realized due to massive passivation and shuttling. Herein, microspheres of a carbon–carbon nitride composite (C@CN) with large mesopores are fabricated via molecular cooperative assembly. Using the C@CN-based electrodes, the effects of the large mesopores and N-functional groups on the electrochemical behavior of sulfur in LSB cells are thoroughly investigated under ultrahigh sulfur-loading conditions ($>15\,mg_S\,cm^{-2}$). Furthermore, for high-energy-density LSBs, the C@CN powders are pelletized into a thick free-standing electrode (thickness: 500 $\mu$m; diameter: 11 mm) via a simple briquette process; here, the total amount of energy stored by the LSB cells is 39 mWh, corresponding to a volumetric energy density of 440 Wh L$^{-1}$ with an areal capacity of 24.9 and 17.5 mAh cm$^{-2}$ at 0.47 and 4.7 mA cm$^{-2}$, respectively (at 24 mg$_S$ cm$^{-2}$). These results have significantly surpassed most recent records due to the synergy among the large mesopores, (poly)sulfide-philic surfaces, and thick electrodes. The developed strategy with its potential for scale-up successfully fills the gap between laboratory-scale cells and

practical cells without sacrificing the high areal capacity and high energy density, providing a solid foundation for the development of practical LSBs.

# 1 | INTRODUCTION

Energy storage systems (ESSs) are essential for the storage of intermittently and stochastically available renewable energy and for the conversion of the stored energy back to electricity, with the aim of serving any predetermined purpose when/where needed. Among various ESSs, batteries are the most widespread energy storage devices for applications in portable electronics, power systems, electric vehicles (EVs), and so forth.[1] They are rated by energy/power density, efficiency, and cycle stability in terms of which the commercial lithium–ion batteries (LIBs) are the highest-ranked technology. LIBs, however, are reaching their physical energy density limits (~240 Wh kg$^{-1}$),[2] which renders them too expensive ($100–200 kWh$^{-1}$)[2] as feasible solutions for medium- or large-scale applications. LIBs also suffer from thermal runaway, calling their future use in the above-mentioned applications into question.[3] This has fueled research into the development of next-generation batteries beyond LIBs, and lithium–sulfur batteries (LSBs) have emerged as one of the most promising candidates.

LSBs use inexpensive and Earth-abundant elemental sulfur ($S_8$) as the cathode active material. On the basis of the redox reaction ($16Li + S_8 \leftrightarrow 8Li_2S$), the multivalent and lightweight sulfur endows LSBs with a high theoretical gravimetric capacity of 1675 mAh g$^{-1}$.[4] Besides, sulfur dissolves well in typical organic solvents like dioxolane and glyme by forming alkali metal polysulfides ($M_2S_x$, M = Li or Na, $2 < x \leq 8$), employing which LSBs feature a wide temperature window and intrinsic overcharge protection, thereby preventing thermal runaway.[5,6] Since Ji et al.[7] demonstrated a gravimetric capacity close to the theoretical value, tremendous research has been conducted in almost all areas of battery development, including the electrode, electrolyte, current collector, separator, and cell configuration. Despite great success over the last decade, LSBs still cannot compete with the benchmark LIBs (~4 mAh cm$^{-2}$), rendering LSBs less attractive.[3] Most previous studies utilized a low sulfur loading (≤2 mg$_S$ cm$^{-2}$), at which even the theoretical LSBs yielded an areal capacity of 3.35 mAh cm$^{-2}$ at 100% utilization. In addition, LSBs operate at ~2 V versus Li/Li$^+$, whereas LIBs operate at ~4.0 V versus Li/Li$^+$, thereby increasing the energy density gap between both battery types.

To progress toward practically viable LSBs, the focus must be placed on high-loading sulfur cathodes.[8] After careful literature surveys and extensive investigations of the state-of-the-art LIB cell (NCR18650B; Panasonic), Hagen et al.[3] proposed a design criterion to develop an LSB that is comparable to the benchmark LIB in terms of volumetric energy density, which exhibited an areal sulfur loading of ≥6 mg$_S$ cm$^{-2}$, sulfur fraction of ≥70 wt%, sulfur utilization of 70% or greater, and electrode thickness of 20 μm per 1 mg$_S$ cm$^{-2}$ when assuming twice the stoichiometric amount of the Li metal anode.[3] In evaluating the gravimetric energy density, the electrolyte volume-to-sulfur weight (E/S) ratio must also be considered because the electrolyte mass contribution is dominant.[9] Very few works presented, to the best of our knowledge, meet all these requirements at the same time. Although it has been argued that a high E/S ratio (>3) is more detrimental to the increase in the energy density than the other parameters, these factors must be addressed as a whole.[7] For example, starting from the trade-off relationship between the sulfur loading and electronic/ionic contact area, the sulfur utilization and cycle stability can then be optimized by using the proper E/S.[10]

It is obvious that the two major technical challenges of LSBs (i.e., shuttling of soluble polysulfides and passivation of charge/discharge products) become more severe under high-loading (≥6 mg$_S$ cm$^{-2}$) conditions, thereby limiting the performance of high-sulfur-loading cathodes.[11] This again engenders the need to rely on a porous carbon support to accommodate a large amount of sulfur and their volume expansion, without losing the electrical/ionic conductivity during charge/discharge cycles. The difference here would be a much higher pore volume and a significantly larger pore diameter than those of the typical porous carbon supports.[12–15] For example, assuming a sulfur fraction of 70 wt% and/or a porous carbon support of 10 wt% in the cathode according to the above-proposed criteria, the pore volume of the carbon support must exceed 2.4 cm$^3$ g$^{-1}$ at 6 mg$_S$ cm$^{-2}$ or greater and 70% utilization. This value must be increased

to $4.3\,cm^3\,g^{-1}$ if we consider 100% conversion of sulfur into $Li_2S$ (Table S1). The pore diameter of the carbon must be increased from a couple of nanometers to, at least, tens of nanometers to achieve such a high pore volume. On the contrary, the pore diameter must be small enough for the loaded sulfur/polysulfides/$Li_2S$ to be in close proximity to the surface of carbon (or electrolyte) and thus remain electrically and ionically conductive. It has been reported that shuttling can be further accelerated by using macroporous carbon supports, reducing the cycle stability and utilization efficiency of the active material.[16,17]

To address all these challenges under ultrahigh sulfur-loading conditions, we herein adopt a carbon-based material with large mesopores; it was prepared by simple molecular cooperative assembly between glucose and triazine molecules, as the main sulfur host. The ratio of glucose to triazine is modified to optimize the pore structure, chemical composition, and electrode design, leading to the desired high pore volume, large pore diameter, abundant surface N-functional groups, and thick electrodes with close-packed particles. A high-conductivity carbon textile or carbon nanotube (CNT) buckypaper is added to the main host as a current collector, thereby providing additional pore volume. In addition, their combination allows us to utilize the conductivity difference for the multistep electrochemical reactions of sulfur, where the highly conductive component mainly induces the high-plateau reactions, and the main host is responsible for the low-plateau reactions. Galvanostatic cycling with potential limitation (GCPL), cyclic voltammetry (CV), ex situ X-ray photoelectron spectroscopy (XPS) analyses, density functional theory (DFT) calculations, and electrochemical impedance spectroscopy (EIS) measurements are conducted to evaluate the electrochemical performance and elucidate the kinetic behavior of sulfur in the combined electrode, which is correlated with the pore structure and chemical composition. Finally, we analyze and optimize the excess cell components to maximize the energy density of the LSBs.

# 2 | EXPERIMENTAL SECTION

## 2.1 | Synthesis of carbon–carbon nitride composite (C@CN)

Melamine (M) (0.5 g), glucose (20.2 g), and cyanuric acid (CA) (0.51 g) were each heated in an oven at 90°C with dimethylsulfoxide (DMSO). In this process, glucose was homogeneously distributed in DMSO, along with M. Both solutions were kept at 90°C for 24 h and mixed together to give white precipitates. MCA and glucose slowly form a hydrogen-bonded network without stirring over the course of 24 h at the same temperature as before. This solution was filtered and washed with ethanol. The resulting white powder of the MCA–glucose complex was dried at 90°C overnight. The reaction product has been denoted as G@MCA-20. G@MCA-20 was purged under $N_2$ atmosphere and then calcined at 600°C for 4 h after increasing the temperature at a ramping rate of 2.3°C $min^{-1}$. The materials collected after cooling are referred to as C@CN or C@CN-20. C@CN-$x$ ($x = 0$–10) samples were also synthesized by using the same method as above.

## 2.2 | Preparation of C@CN electrode by slurry casting process

A commercial carbon cloth (CC) with a diameter of 14 mm (CH900-20, 21 mg; Kuractive, Kuraray Chemical Co., Ltd.) was used as the current collector, and C@CN-CC electrodes were fabricated by a slurry casting process. C@CN powders, Super P as a conductive agent, and poly (vinylidene fluoride) binder were mixed in a mass ratio of 80:10:10 and homogenized in N-methyl-2-pyrrolidone. Homogeneous slurries were uniformly cast on the CC and dried at 150°C for 24 h.

## 2.3 | Preparation of pC@CN

G@MCA powder mixed with 2 mg of multi-wall carbon nanotube (acting as additional conductive material) was pressed into a pellet of 150 mg with a diameter of 13 mm and a thickness of 950 $\mu$m at 20 MPa. This pellet was heated at 600°C at the same ramping rate as used in the C@CN manufacturing process. As a result, the generated pC@CN (pelletized C@CN) electrode with a diameter of 11 mm contained 10 mg of C@CN and the same mass of multi-wall carbon nanotube as before heating.

## 2.4 | Material characterization

Powder X-ray diffraction (XRD) measurements were performed using a Rigaku D/max Ultima III (Rigaku) instrument with Cu-K$\alpha$ radiation at the Center for Research Facilities at the Chonnam National University (CCRF). Field-emission scanning electron microscopy observations (SU-70, 15.0 kV; Hitachi) was performed at the Korea Basic Science Institute (KBSI). Nitrogen sorption analysis was carried out at a temperature of 77 K using a Micromeritics ASAP 2020 analyzer. Raman

spectroscopy was performed on an Aberration-corrected Czerny–Turner monochromator in CCRF. Thermogravimetric analysis (TGA-50) was conducted under a flow of $N_2$ in the temperature range of 25–900°C at a heating rate of 10°C $min^{-1}$. Fourier-transform infrared (FT-IR) spectra were recorded using a JACSO FT-IR 4100 spectrometer. High-resolution transmission electron microscopy (HR-TEM) images were obtained using EM912 (120 kV, Carl Zeiss). XPS data were obtained on a Thermo Scientific K-Alpha XPS spectrometer (CCRF) with a monochromatized, microfocused Al-K$\alpha$ line source. Solid-state $^{13}C$ cross-polarization magic angle spinning (CP-MAS) nuclear magnetic resonance (NMR) spectra were collected on a JNM-ECZ400R/S3 instrument.

## 2.5 | Electrochemical measurements

The blank electrolyte is 1 M lithium bis(trifluoromethanesulfonyl) imide (LiTFSI; 99.95% from Sigma-Aldrich) dissolved in 1,3-dioxolane (DOL; 99.8% from Sigma-Aldrich) and 1,2-dimethoxyethane (DME; 99.5% from Sigma-Aldrich) (1:1 volume/volume) with lithium nitrate (LiNO$_3$; 99.99% from Sigma-Aldrich, 1wt %). Elemental sulfur (99.5% from Sigma-Aldrich) and Li$_2$S (99.9% from Alfa-Aesar) were mixed in blank electrolyte and heated at 50°C to prepare the catholyte (1 M Li$_2$S$_6$) as a sulfur source. The catholyte was applied to the electrode during cell assembly without additional steps in the preparation of sulfur composite. Cells were assembled in an argon-filled glove box (below 0.1 ppm of O$_2$ and H$_2$O concentration). The catholyte was immersed in the above-mentioned cathodes (CC, C@CN-CC, pC@CN-CC, pC@CN-CNT), to which the blank electrolyte was added. Then, the polypropylene (PP) separator with a diameter of 19 mm (ceramic-coated membrane) and lithium metal with a diameter of 10 mm were sequentially placed on top of the cathode.

## 2.6 | DFT calculation

Spin-polarized calculations were performed using the projector-augmented wave method, as implemented in VASP. We used the Perdew–Burke–Ernzerhof (PBE) exchange-correlation functional and Grimme's D3 correction with zero dampings. Supercells with lattice sizes of $27 \times 24 \times 20$ Å and $26 \times 30 \times 20$ Å were used for g-CN and graphene, respectively, to minimize fictitious interactions between neighboring images. An energy cutoff of 400 eV and gamma-centered single k-point were used with convergence criteria of 10–6 eV and 0.05 eV A$^{-1}$.

The adsorption sites were explored by varying the position and angle of the adsorbate molecules, and the most stable geometry was used for evaluating the binding energy.

# 3 | RESULTS AND DISCUSSION

## 3.1 | Synthesis of G@MCA

M and CA form spherical crystal aggregates (MCA) in DMSO. During crystallization, MCA grows in the xy-plane via extensive hydrogen bonding, yielding a two-dimensional (2D) network, and simultaneously stacks along the z-axis via van der Waals interactions between the 2D networks. The former precedes the latter at room temperature, leading to the formation of plate-like microparticles. Such directional growth can be tailored by modifying the intermolecular interactions. For example, the DMSO solvent itself can act as a hydrogen bonding acceptor for the −NH$_2$ of M at elevated temperatures due to the increased solubility of M (or formation of an M–DMSO solvation shell) and disrupt the formation of MCA, whereas the van der Waals interaction between the 2D networks remains intact. This results in preferential growth along the z-axis, thus forming hexagonal microfibers.

In a similar way, we intended to modify the growth of MCA and then utilize it as a precursor to generate a porous C@CN with a high pore volume, appropriate for a high-sulfur-loading cathode. Glucose with five hydroxyl groups and one ethoxide group was introduced as a structure-directing agent and an additional carbon source, where glucose binds to MCA to generate an MCA–glucose composite precursor (G@MCA) and also modifies the growth of MCA by competing with CA for hydrogen bonding. Notably, G@MCA was designed to have a uniform shape and size to facilitate agglomeration into dense spherical particles and subsequent transformation into spherical particles based on both carbon and carbon nitride with sufficient pore volume during carbonization. The overall synthesis procedure is shown in Scheme 1.

To assess the effect of glucose on the molecular interaction between M and CA, different amounts of glucose were added to the DMSO solution and the morphology of MCA was observed, reflecting the change in the crystal structure. The resulting materials are referred to as G@MCA-x (x = 0, 10, and 20), where x is the mass ratio of glucose to MCA. Our focus was mainly on G@MCA-20 and the corresponding C@CN-20, because the properties of these materials are appropriate for the (ultra)high areal sulfur-loading conditions, as
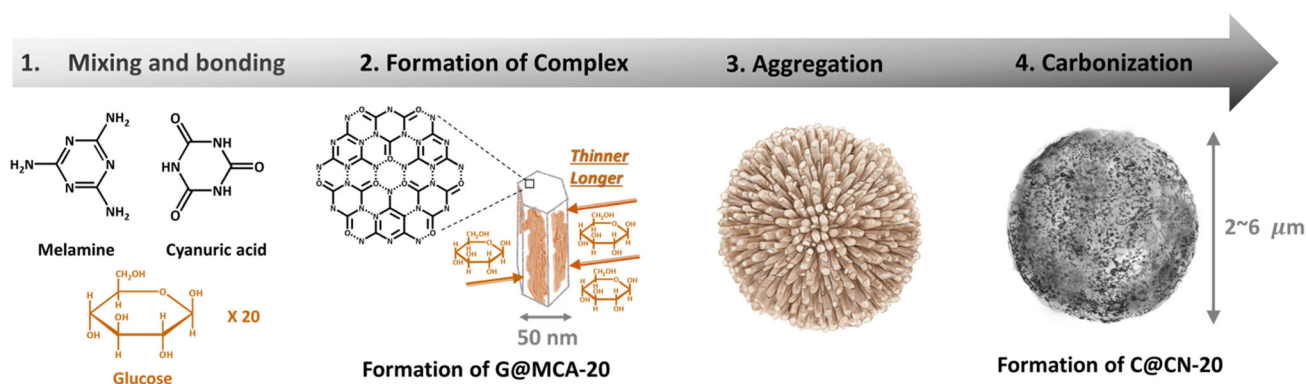
**SCHEME 1** Molecular cooperative assembly-based synthesis of C@CN-20. C@CN, carbon–carbon nitride composite; CA, cyanuric acid; G@MCA, MCA–glucose composite; M, melamine

shown below. Other samples were included only when evaluating the effect of the glucose content.

The scanning electron microscopy (SEM) images show that the irregular plates/rod-like particles gradually became uniform nanofibers with increasing glucose content (Figure S1). In the G@MCA-20 sample, MCA eventually formed nanofibers with a thickness of 50 nm and a length of roughly 0.45 μm, which agglomerated into sea urchin-like spherical microparticles with a size of 7 μm.

All of the powder XRD patterns of G@MCA show four strong peaks at 10.63, 18.45, 21.48, and 27.59° corresponding to the (100), (110), (200), and (002) reflections, respectively. This reveals that the in-plane 2D hexagonal ordering of the MCA network and their graphitic stacking of the layers with an interlayer distance of 0.32 nm remained almost intact irrespective of the presence of glucose (Figure S2). Slight broadening of the (002) peak and the decrease in the intensity ratio of the (100) to (002) peaks in the XRD pattern of G@MCA-20 are attributed to the formation of nanofibers with small 2D MCA. In addition, the FT-IR spectra of G@MCA-20 show the C=O vibrational bands at 1732 and 1780 cm$^{-1}$ and the triazine ring vibration of M at 765 cm$^{-1}$. The typical C=O band of CA and the triazine ring vibration of M are observed at 1696/1755 and 808 cm$^{-1}$, respectively; these bands are, respectively, shifted to higher frequency and lower frequency as a result of hydrogen bonding of the N–H···O and N–H···N linkages.[18] It is thus believed that although they are interrupted, the intermolecular interactions between M and CA are still strong enough to form the same crystalline structure. Instead of forming a molecular cooperative assembly with MCA, glucose terminates further extension of the 2D network by attaching to the surface of the seed crystals. The cyclic structure of glucose is twisted in three dimensions and has multiple out-of-plane functional groups with a trans arrangement,

which makes its involvement in the process of forming a planar crystal difficult.

## 3.2 | Synthesis of C@CN

G@MCA was heated to 600°C to generate the desired C@CN. The structure differed depending on the amount of glucose: The higher the glucose content, the denser the particles (Figure S3). Glucose serves to increase the mass yield and thus retain the framework during carbonization (Figure S4). Glucose and its carbonization product are not only thermally stable, but they also mitigate the mass loss of MCA during thermal polycondensation, increasing the contribution of the peak at 27° in the XRD pattern, attributed to MCA-derived g-CN (Figure S5). This observation is similar to the improved degree of polycondensation of g-CN confined in a nanoporous alumina membrane or molecular crystals.[18]

The resulting black powder of C@CN-20 consists essentially of uniform spherical microparticles with a diameter of 2–6 μm and inherits the parent morphology of the precursor (G@MCA-20) with ~30% shrinkage in the diameter (Figures 1A and S1). Some broken particles reveal that these are solid spheres, whose walls consist of interconnected nanoparticles with dimensions of 38–70 nm; the particles also have pores of around 35 nm (Figure 1B). Particles of C@CN-20 have a similar texture (shape and size) to that observed in C@CN-0–10, possibly indicating that these particles are polycondensation products of MCA, that is, a polymeric melon. N$_2$ sorption analysis was used to probe the pore structure. The Brunauer–Emmett–Teller surface area of C@CN-20 is 316 m$^2$ g$^{-1}$, with a pore volume of 1.96 cm$^3$ g$^{-1}$ (Figure 1D). The pore size distribution calculated from the adsorption curve by using the Barrett-Joyner-Halenda method was centered at 35 nm, which is in good
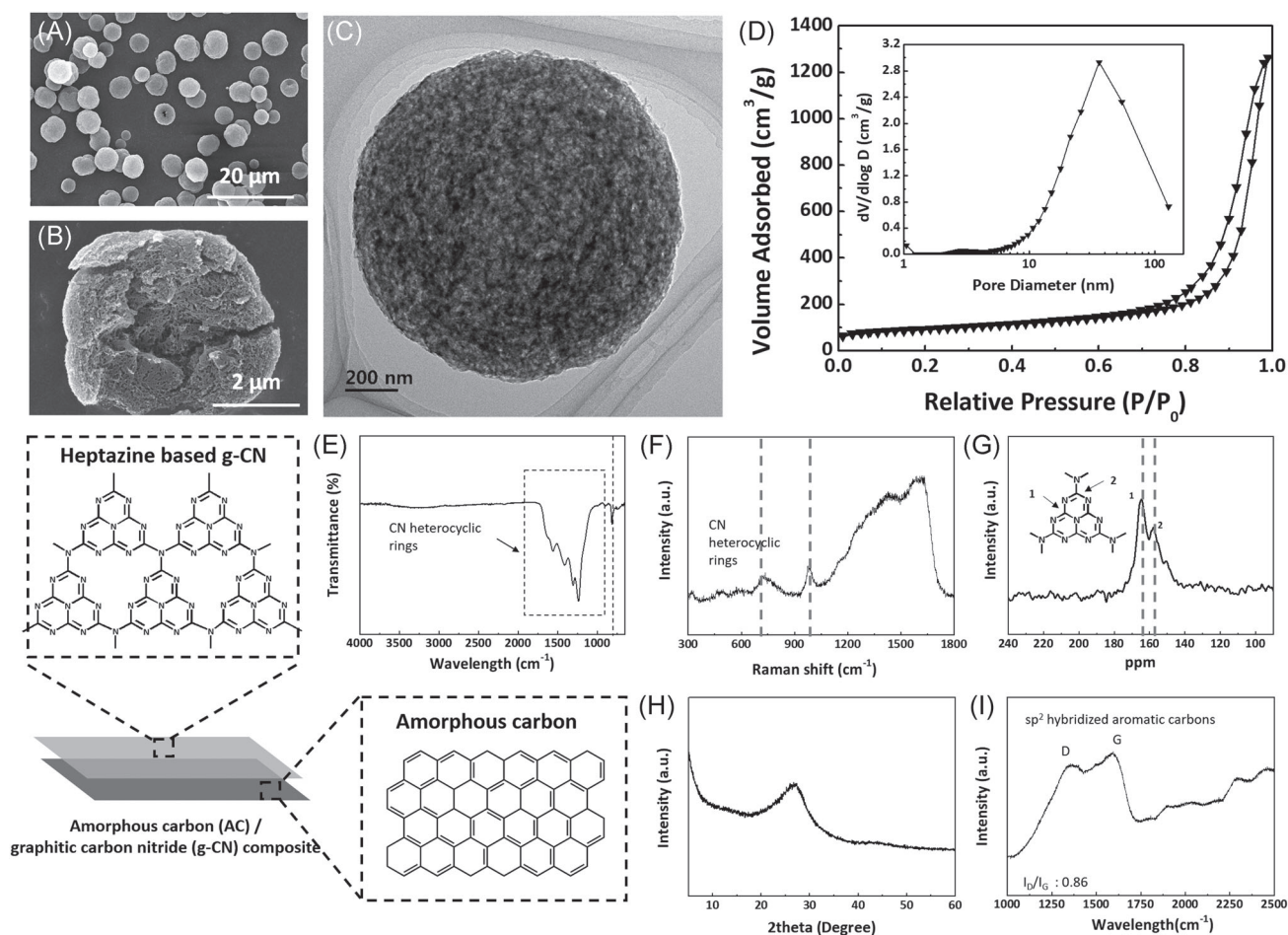
**FIGURE 1** (A–C) Scanning electron microscopy and transmission electron microscopy images, (D) N$_2$ sorption isotherm (inset: pore size distribution), (E) Fourier-transform infrared spectrum, (F) ultraviolet (UV) Raman spectrum (excitation wavelength: 325 nm), (G) solid-state $^{13}$C cross-polarization magic-angle spinning nuclear magnetic resonance spectrum, (H) powder X-ray diffraction pattern, and (I) visible Raman spectrum (excitation wavelength: 512 nm) of carbon–carbon nitride composite (C@CN)-20

agreement with the TEM observation (Figure 1C). The number of pores with diameters of 20–60 nm increases significantly as the amount of glucose increases (Figure S6). Also, we observed that powder color changes from dark yellow to black with increasing glucose content (Figure S7).

To determine whether MCA and glucose merge into the N-containing carbons or undergo independent thermal polycondensation and carbonization, C@CN-20 was analyzed by elemental analysis (EA), XRD, FT-IR, UV Raman, and solid-state $^{13}$C CP-MAS NMR spectroscopy. The data show that C@CN-20 contains g-CN moieties as a result of independent polycondensation. CN heterocyclic rings are observed in the FT-IR spectrum (Figure 1E): The multiple peaks in the region of 1200–1650 cm$^{-1}$ correspond to the stretching mode of the CN heterocyclic rings and the peaks around 810 cm$^{-1}$ are attributed to the breathing mode of the triazine ring.[18,19] This is further supported by the UV Raman spectrum, showing two strong peaks at 702 and 990 cm$^{-1}$, associated with the breathing modes of the triazine ring

(Figure 1F).[20] More precisely, C@CN-20 contains tri-*s*-triazine, the typical structural motif of the polymeric melon prepared by thermal polycondensation of N-rich molecular precursors, as is shown in the $^{13}$C NMR spectrum.[21] The two distinct peaks at 164.3 and 157 ppm are assigned to the C–N$_3$ and CN$_2$(NH$_x$) groups of the tri-*s*-triazine molecules linked by trigonal N or −NH$_x$, respectively (Figure 1G).

The carbonization product also has the characteristic structure of amorphous carbon. The XRD pattern of C@CN-20 shows a broad peak at approximately 26.1° (Figure 1H). The high-resolution C 1s XPS spectrum shows a peak at 284.8 eV, corresponding to C–C or C═C (Figure S8). In addition, the D and G peaks in the visible Raman spectrum appear around 1366 and 1592 cm$^{-1}$, corresponding to the breathing mode of A$_{1g}$ symmetry and the in-plane bond stretching motion of E$_{2g}$ symmetry, respectively, of the $sp^2$-hybridized aromatic carbons (Figure 1I).[22] The carbon content in the C@CN samples gradually increases with the initial glucose content (Figure S9). C@CN-20 has an average

carbon content of 49 wt%, which is 19 wt% higher than that of C@CN-0 (~30 wt%). This indicates that glucose is indeed included in the composite precursor and carbonized during heat treatment. As glucose is localized mainly at the surface of the composite precursor, the surface carbon content (58.5 wt%) determined from the XPS survey scan is ~9.5 wt% higher than the average value (Table S2).

## 3.3 | Electrochemical characterization of C@CN

To evaluate the electrochemical performance, C@CN was first loaded on a commercial CC current collector with an areal loading of 4 mg cm$^{-2}$. C@CN-20 is referred to as C@CN unless the mass ratio is indicated. The cathode (C@CN-CC) was combined with a metallic lithium anode and 1 M LiTFSI solution in 1,3-dioxolane and 1,2-dimethoxyethane (1:1 volume/volume) electrolyte in a CR2032 coin cell for CV, GCPL, and EIS measurements. The high-sulfur-loading capability of C@CN was first evaluated by the GCPL technique with increasing the areal sulfur loading from 2 to 15 mg$_S$ cm$^{-2}$ at a constant areal current density of 3 mA cm$^{-2}$. Figure 2A–D shows the areal sulfur loading-dependent GCPL profiles of C@CN-CC; the corresponding data for CC alone are presented for comparison. Typical plateaus appear even at 15 mg$_S$ cm$^{-2}$ without severe polarization upon cycling: Two plateaus corresponding to the reduction of high (Li$_2$S$_x$, $4 \leq x \leq 8$) and low (Li$_2$S$_x$, $1 \leq x < 4$) polysulfides are clearly observed at 2.2 and 2.0 V versus Li/Li$^+$ in the discharge profile over 50 cycles, respectively, and the ensuing charge profiles show a plateau around 2.3 V versus Li/Li$^+$, followed by a gradual slope toward the high potential limit (2.6 V vs. Li/Li$^+$) (Figure S10). The areal capacity of C@CN-CC gradually increases from 2 to 8.5 mAh cm$^{-2}$ when the areal sulfur loading increases from 2 to 10 mg$_S$ cm$^{-2}$. These capacity values correspond to sulfur utilization efficiencies of 60% and 50%, respectively. Above 10 mg$_S$ cm$^{-2}$, the areal capacity increases slightly, the utilization efficiency decreases abruptly to 30%, and finally, the cycle stability rapidly deteriorates within 20 cycles, indicating that the C@CN-CC electrode has a certain sulfur-loading limit, for example, 10 mg$_S$ cm$^{-2}$ (Figure 2E,F). We attribute this to the well-known surface passivation of CC by insoluble lithium sulfide (Li$_2$S). Micropores aligned parallel within CC are passivation-prone, as we previously reported.[23] Indeed, the discharge profiles of CC alone are sloping with an ill-defined lower potential plateau, and the capacity generation is the lowest, especially at >10 mg$_S$ cm$^{-2}$ (Figure 2).

It is clear from the above comparison that C@CN is crucial for developing the lower potential plateau and thereby increasing the total capacity at 10 mg$_S$ cm$^{-2}$ or lesser, whereas the higher potential plateaus almost overlap each
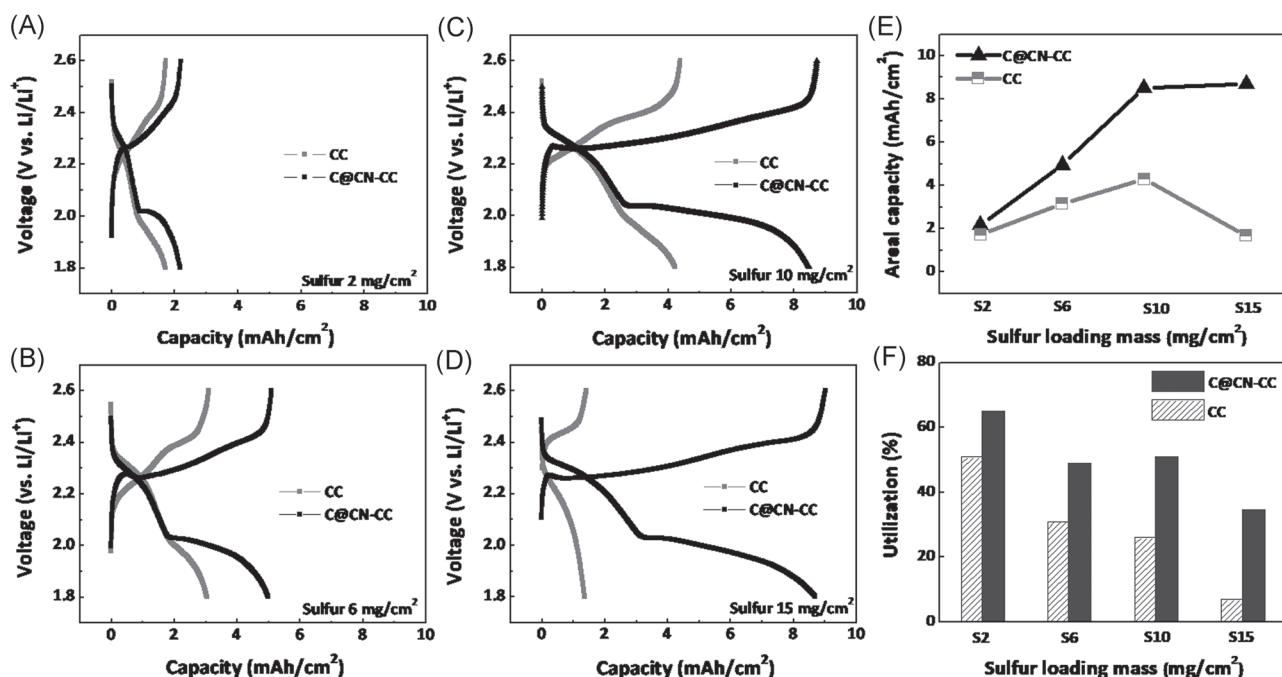


**FIGURE 2** Charge/discharge profiles of carbon–carbon nitride composite (C@CN)-carbon cloth (CC) and CC electrodes after 10 cycles: (A) 2 mg$_S$ cm$^{-2}$, (B) 6 mg$_S$ cm$^{-2}$, (C) 10 mg$_S$ cm$^{-2}$, and (D) 15 mg$_S$ cm$^{-2}$. Comparison of electrochemical performance depending on areal sulfur loading: (E) areal capacity and (F) sulfur utilization efficiency. All tests were conducted at 3 mA cm$^{-2}$

other, irrespective of the presence of C@CN. The lower potential plateau in the discharge profiles becomes more prominent with increasing sulfur loading: The ratio of the lower potential plateau capacity to that of the higher potential plateau gradually increases from 1.5 to 2.4, which is close to the theoretical value (3.0), with increasing sulfur loading. The capacity ratio of CC alone, however, remains at 1.0, irrespective of the sulfur loading, although the total capacity increases slightly (Figure S11). These results are consistent with the CV results: The peak current density of the lower potential plateau around 2.0 V versus Li/Li$^+$ is four times higher in the presence of C@CN, especially at 10 mg cm$^{-2}$, whereas the peak current density of the higher potential plateau in the CV curves remains the same, irrespective of the presence of C@CN (Figure S12).

CC has a sufficiently high pore volume to accommodate up to 15 mg$_S$ cm$^{-2}$ sulfur when assuming complete conversion (Figure S20 and Table S3). The simple correlation between the pore volume and capacity generation is thus invalid at such high sulfur loadings. This suggests that there must be another factor that governs the electrochemical performance of the C@CN-CC electrode in LSBs. By comparing the GCPL results for the C@CN-5–20 samples, it was deduced that the large mesopores are mainly responsible for developing the lower

potential plateaus and high sulfur-loading capability of C@CN-CC (Figure S13). It can easily be seen that the capacity of the lower potential plateau (or the capacity ratio) is proportional to the mesopore volume of around 35 nm. The capacity ratio increases from 0.6 to 2.0 when $x$ for C@CN–$x$ increases from 0 to 20. This was further corroborated by the GCPL behavior of the CC electrode loaded with Super P conductive carbon additive (~80 nm, 4 mgC cm$^{-2}$) (Figure S14). The plateau potentials and capacity generation of CC are only minimally affected by the additional Super P particles, without the generation of any internal porous structures.

However, the capacity at the higher potential plateau of the C@CN-$x$-CC electrodes remains almost the same at 2.5 mAh cm$^{-2}$, which matches well with the above GCPL results for C@CN-CC with different areal sulfur loadings. In addition, the limit of the areal sulfur loading is determined by the volume of added C@CN (Figure S15). The difference in the kinetic behavior of C@CN-CC and CC was also revealed by measuring the peak current density with a variation of the CV sweep rate (Figure 3A–D). Assuming that the current at any potential is generally dominated by either a capacitive or faradaic process, the following power-law equation for the relation between the measured current and the sweep rate was established:
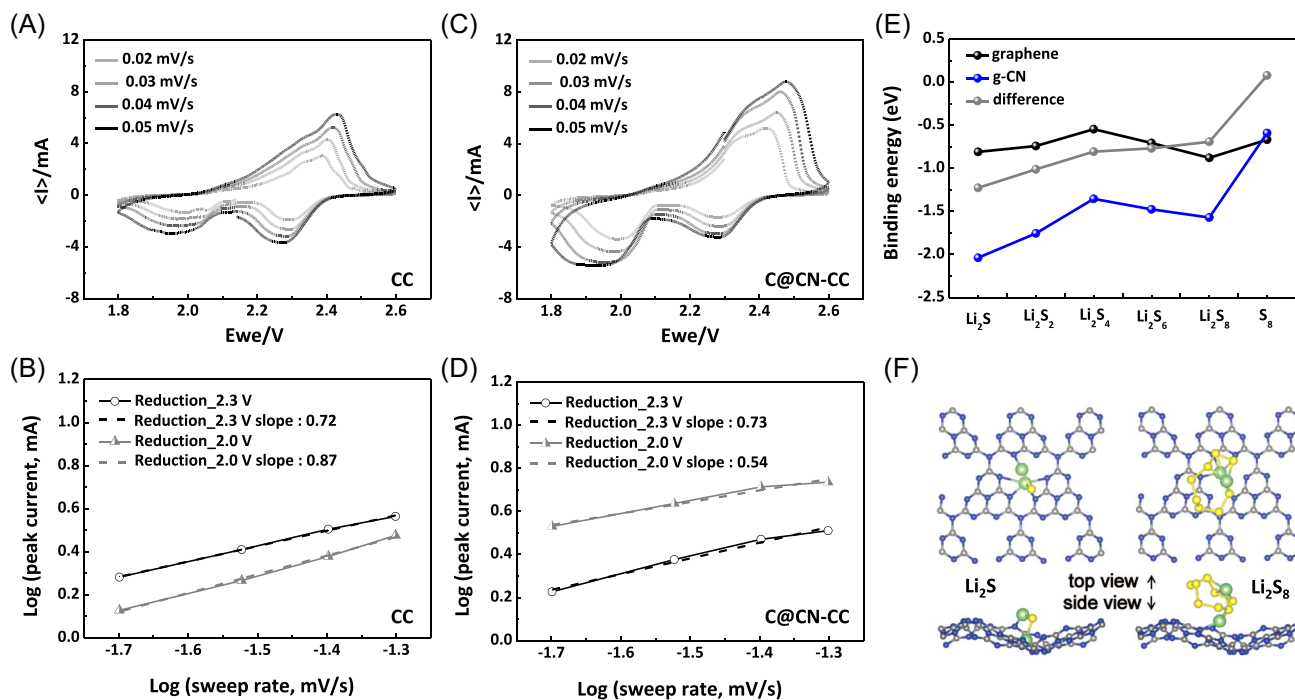


**FIGURE 3** Cyclic voltammetry curves and the corresponding log(current) versus log(sweep rate) plot of (A, B) carbon cloth (CC) and (C, D) carbon nitride composite (C@CN)-CC electrodes at 10 mg$_S$ cm$^{-2}$ and scan rate in the range between 0.02 and 0.05 mV s$^{-1}$. (E) Binding energy with Li$_2$S$_x$ molecules on the g-CN surface in comparison with graphene. (F) The most stable configurations of Li$_2$S and Li$_2$S$_8$ and on g-CN, carbon (C), nitrogen (N), sulfur (S), and lithium (Li) elements are shown in gray, blue, yellow, and green, respectively, in the models

$$I = a\nu^b.$$

The so-called $b$ value is generally estimated by least-squares fitting of $I$ versus $\nu$ for given surface potential values and is expected to vary between $b = 0.5$, in the case of a Faradaic current or semi-infinite linear diffusion, and $b = 1$, for purely capacitive behavior or non-diffusion-controlled charge storage. It was estimated from these results that the reduction reaction of low polysulfides is mainly governed by solid-state diffusion in C@CN-CC ($b = 0.54$) and surface reaction ($b = 0.87$) for CC (Table S5). However, in the reduction reaction of high polysulfides, the $b$ values of C@CN ($b = 0.73$) and CC ($b = 0.72$) are close to each other. Thus, it is not too controversial to assume that the high polysulfides are mainly reduced in the micropores of CC, after which the low polysulfides are reduced in the large mesopores of C@CN, where the high solubility of the high polysulfides in the liquid electrolyte facilitates the transfer of the active material between the two different supporting materials (or pore systems) by diffusion. Similar behavior of polysulfides has recently been reported by Chung et al.[24] They found that separating the roles of the highly conductive component and sulfur retention component is an efficient way to build high-performance LSBs with high energy density and high cycle stability.

To further clarify this assumption, C@CN-CC was subjected to potential-wise ex situ XPS analyses. Compared with the pristine polysulfides stored at OCV (~2.3 V vs. Li/Li$^+$), that is, Li$_2$S$_6$, more reduced and more oxidized sulfur species with binding energies closer to those of sulfur and Li$_2$S, respectively, are clearly found in the C@CN-CC electrode discharged to 1.8 V versus Li/Li$^+$ and charged to 2.6 V versus Li/Li$^+$ (Figure S16). The discharge products or the pristine polysulfides are, however, negligible in CC due to their removal during the washing step. The reduction does not proceed further than the soluble species in the CC. This indicates the surface affinity of C@CN for soluble polysulfides enables further reduction in close proximity to the surface, where this process is obviously superior to the physical adsorption on the micropores in CC.

DFT calculations revealed that such affinity is probably conferred by the tri-s-triazine moieties of g-CN. Figure 3E shows the binding energies of sulfur (S$_8$ ring) and lithium polysulfides (LiPS) (Li$_2$S$_x$, where $x = 1, 2, 4, 6$, and 8) on graphene and g-CN. On the graphene surface, all sulfide molecules exhibit small and similar binding energies (from −0.55 to −0.88 eV) due to the nonpolar surface of graphene. In contrast, on the g-CN surface, the binding energy is much stronger (from −0.59 to −2.04 eV) due to the strong ionic bond between Li and N, as displayed in Figure 3F and S17a. This moderate binding energy is similar to that of transition metal sulfides, such as TiS$_2$, ZrS$_2$, and VS$_2$,[25] which have been verified to be efficient anchoring materials, indicating that g-CN is an adequate nonpolar surface for capturing LiPS. In addition, the binding energy of LiPS on g-CN increases with decreasing chain length ($x$); this can be more clearly identified from the plot of the binding energy difference for g-CN with respect to graphene. This behavior is analogous to that of the TiN-decorated carbon cathode,[26] where it is suggested that TiN promotes the fragmentation of LiPS and formation of the solid-phase product, and also acts as an anchor for these species. Considering that TiN also extends the capacity in the lower voltage region, like the present g-CN, we anticipate that g-CN should play a role similar to that of TiN. The surface functional groups are thus helpful in improving the electrical/ionic contact among the sulfur species, supporting material/current collector, and electrolyte. Indeed, strong binding of Li$_2$S$_6$ to the C@CN is demonstrated by the disappearance of brownish color and a broad peak around 350 nm in UV–Vis spectra of Li$_2$S$_6$ solution in DOL:DME (1:1 volume/volume) (Figure S17b). Also, the charge transfer resistance ($R_{ct}$), reflecting the interface between the electrolyte and electrode, remains low (below 5 Ω cm$^2$) irrespective of the sulfur loading, as shown in the EIS results (Figure S18 and Table S6).[27]

## 3.4 | Optimizing the cell toward high energy density

It is obvious that higher areal sulfur loading or areal capacity is better. The question remains: How high an areal loading or areal capacity do we need to achieve?

The areal capacity versus areal current density plot (with areal sulfur loading) was constructed to specify the first performance benchmark. It can be seen that C@CN-CC is poorer than most carbon-based sulfur cathodes recently reported in every aspect of concern: areal sulfur loading, areal current density, and areal capacity (Figure S19). To compete with the reported materials in terms of performance, the areal capacity first needs to be further increased to 15 mAh cm$^{-2}$ or higher. Assuming a sulfur utilization efficiency of 40%, which is the typical value for ultrahigh sulfur-loading cathodes (>15 mg$_S$ cm$^{-2}$), achieving an areal capacity of 16 mAh cm$^{-2}$ or higher requires an areal sulfur loading of 24 mg$_S$ cm$^{-2}$ or higher and, in turn, areal C@CN loading of 10 mg cm$^{-2}$ or higher (Figure S20 and Tables S3 and S4).

Slurry casting cannot provide C@CN-CC electrodes with the required working parameters in the loading ranges (neither 15 mg$_S$ cm$^{-2}$ nor >4 mg C@CN cm$^{-2}$), prompting us to utilize the briquette process

(Figure S21).[28] G@MCA-20 powder could simply be pressed into a pellet at 20 MPa, where sticky glucose plays the role of a binder. Heating the pellet at 600°C generates a free-standing pelletized C@CN (pC@CN) electrode (Figure S22). Notably, the resulting pC@CN retains the structural and chemical properties of C@CN, as evidenced by the largely similar $N_2$ sorption, XRD, high-resolution N 1s XPS, and FT-IR profiles (Figure S23). The pC@CN pellet at a loading of $10 \, mg \, cm^{-2}$ has a diameter of 10 mm and 500-μm thickness, where these parameters could be tuned by simply changing the initial mass loading of G@MCA-20 powder or possibly modifying the shape and size of the pellet die (Table S7). This shows great potential for scale-up of thickness and meets the design criteria ($\geq 300 \, \mu m$) of the thick electrode suggested for the cost-effective manufacture of battery cells for applications in EVs and ESSs.[29–31] Further cost reduction and performance improvement are naturally expected due to the removal of the use of the polymer binder and solution-based electrode fabrication procedures. Furthermore, the soft G@MCA particles with fairly uniform size distribution enable the C@CN microparticles to make multiple physical contacts with one another under pressure; however, this process leaves dents at the point of contact between the spherical microparticles (Figure S24). Such contacts with close-packed features facilitate homogeneous electron/ion distribution over the thick pC@CN. As shown in the schematic diagram, pC@CN was combined with CC in a CR2032 coin cell for the GCPL test (Figure S25). pC@CN was simply placed between the CC and PP separators without any further treatment, which simplifies the electrode fabrication procedures. The difference in the conductivity of CC and pC@CN induces the initial formation of the reaction front on the surface of CC, which is the conductive part. The reaction front then gradually moves toward the thick pC@CN with pore tortuosity, which is the retention part, via diffusion. This is favorable for both efficient electrochemical reactions and stable retention of high polysulfides (Tables S8 and S9).

At an areal current density of $4.7 \, mA \, cm^{-2}$, the areal capacity of pC@CN-CC increases to ~16.5 mAh cm$^{-2}$ at $24 \, mg_S \, cm^{-2}$ and ~19 mAh cm$^{-2}$ at $30 \, mg_S \, cm^{-2}$, both of which already meet the above-mentioned requirements and are unachievable numbers for C@CN-CC (Figure S26). It should be noted that CC (or pC@CN) alone generates negligible capacity (~2 mAh cm$^{-2}$) under the same conditions, as neither of them gives rise to the lower (or higher) plateau, revealing the separated roles. Thus, pC@CN assists the CC to treat high polysulfides, and at least partly recovers the capacity generation (~6 mAh cm$^{-2}$) from the higher plateau (Figure S27).

This again confirms our assumption that a high loading of C@CN in the combined electrode is a critical factor for improving the GCPL performance under ultrahigh sulfur-loading conditions.

The utilization efficiency of sulfur is, however, only 41% at $24 \, mg_S \, cm^{-2}$ or higher. This is attributed to the substantial passivation of CC. More precisely, the difficulty in efficiently distributing the soluble high polysulfides into pC@CN in large quantities precludes the subsequent reaction occurring at pC@CN in the lower potential ranges, leading to a severe polarization of about 200 mV for the lower plateau and a lower capacity ratio of ~1. A low areal current density of, for example, $0.47 \, mA \, cm^{-2}$, provides more time for high polysulfides to diffuse into pC@CN, which further increases the areal capacity of pC@CN-CC up to 24.7 mAh cm$^{-2}$, corresponding to a utilization efficiency of 61% at $24 \, mg_S \, cm^{-2}$ (Figure S28). The improvement (50%) driven by the low current density is mainly seen in the lower plateau region: The capacity generated by the high and low polysulfides increases by 28% and 65%, respectively, in comparison to those at $4.7 \, mA \, cm^{-2}$, and the capacity ratio increases to 1.8 with minimal polarization. These results suggest that the conductive and retention components must be harmonized (or optimized) in terms of the reaction and mass-transfer rates of the high polysulfides to achieve efficient relay. In other words, instead of finishing the entire reduction procedure quickly, leading to severe passivation, the use of CC induces the partial treatment of the high polysulfides and then allows them to diffuse (or shuttle) into pC@CN to complete the rest of the multi-step reactions. The harmonization is, however, a tricky task, as pC@CN-CC only allows a narrow current density window owing to the limited mass transfer in microporous CC, especially under ultrahigh sulfur-loading conditions.[32] This prompts us to simply switch from microporous CC to meso- and macro-porous CNT buckypaper with which we intend to increase the mass-transfer rates (or shuttling) of the high polysulfides in the pores, increasing the contribution of pC@CN for capacity generation (Figure S29). It should be noted that it is beyond the scope of this study to optimize the mass-transfer rate of high polysulfides in liquid electrolytes involving diffusion and reaction.

pC@CN-CNT generates an areal capacity of 16.4 mAh cm$^{-2}$, which is comparable to that of pC@CN-CC at $24 \, mg_S \, cm^{-2}$ and $4.7 \, mA \, cm^{-2}$, as shown in Figure 4B, which also presents the GCPL data for CNT paper alone under the same conditions. Despite the much lower surface area (230 vs. 1600 m$^2$ g$^{-1}$) of CNT paper, the combined electrode showed only a marginal loss of ~2.5 mAh cm$^{-2}$ in the capacity generation at the

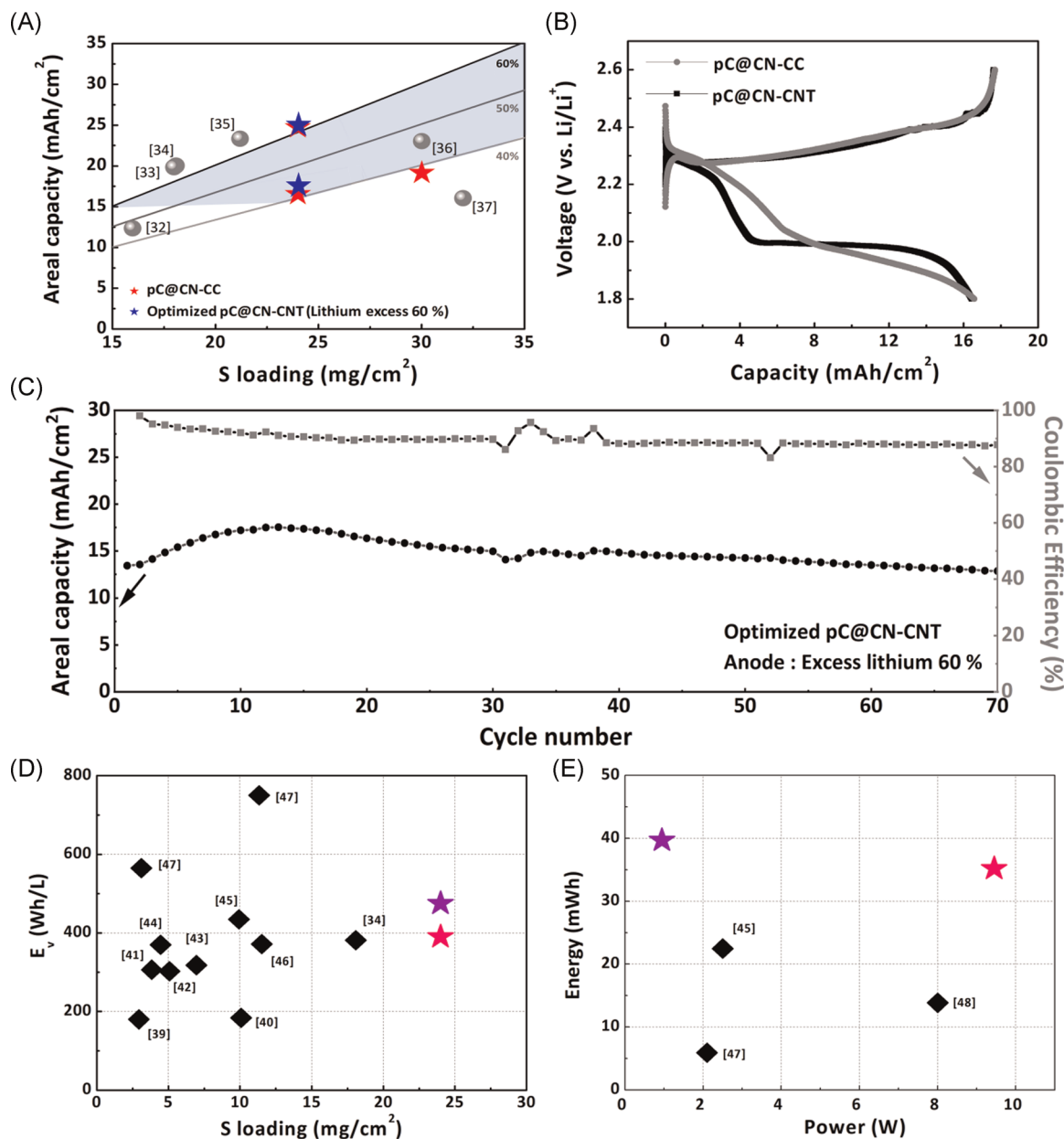**FIGURE 4** (A) Areal capacity versus areal sulfur loading, (B) pelletized carbon nitride composite (pC@CN)-carbon nanotube (CNT) electrode at 24 mg$_S$ cm$^{-2}$ after 10 cycles, (C) cycle stability of optimized pC@CN-CNT cell, (D) volumetric energy density (Ev) versus areal sulfur loading, and (E) total amount of energy stored (mWh) versus power (W). The volumetric energy density for the literature data was calculated according to Xue's method[33]

higher plateau, justifying our strategy toward achieving high areal capacity. This approach increases the areal mass loading of the retention component rather than the conductive component in response to the ultrahigh sulfur-loading conditions. Furthermore, pC@CN-CNT features an ideal charge/discharge profile with a capacity ratio of 2.6, which is close to the ideal value, and a clear plateau at 4.7 mA cm$^{-2}$. This corroborates our assumption that pC@CN (or CNT paper) suffers minimally from passivation under ultrahigh sulfur-loading and high current density conditions due to the large pore size.

For pC@CN-CC or -CNT, the areal capacity increases with the areal sulfur loading and, in turn, the areal pC@CN loading. This inevitably makes pC@CN thicker and thicker, which may cause the resulting high areal capacity electrode to be "disguised" as a high-energy-density electrode. This unintended deceptive appearance of the thick sulfur electrode can be detected by comparing it with other systems in terms of volumetric energy density as well as areal capacity (Figure S30). Thus, the energy density plot specifies the second benchmark, 350 Wh L$^{-1}$.

pC@CN-CC has a volumetric energy density of $130\,Wh\,L^{-1}$ at $24\,mg_S\,cm^{-2}$, where we only considered the volume of the Li metal anode, PP separator, and polysulfide-infiltrated pC@CN-CC cathode. Although the areal capacity is close to the current record ($23.3\,mAh\,cm^{-2}$ at $3.5\,mA\,cm^{-2}$), it is far below the benchmark energy density ($350\,Wh\,L^{-1}$) of the prototype LSB built by Sion power and those ($350–750\,Wh\,L^{-1}$) of carbon-based cathodes recently reported (Figure 4D). Cell component analysis indicates that thick CC and excess Li metal, occupying about 31% and 47% of the total cell volume, are mainly responsible for the low value (Figure S31). Volume reduction of these species was thus carried out at $4.7\,mA\,cm^{-2}$ and $24\,mg_S\,cm^{-2}$. Switching from thick CC to thin CNT paper increases the volumetric energy density to $180\,Wh\,L^{-1}$. Then, the 75% decrease in the volume of lithium metal, which is initially 6.4 times more than the theoretical amount required for $24\,mg_S\,cm^{-2}$, enables the pC@CN-CNT cell to achieve a volumetric energy density of $390\,Wh\,L^{-1}$, surpassing the second benchmark. The resulting pC@CN-CNT cell delivers a maximum areal capacity of $17.5\,mAh\,cm^{-2}$ and a reversible capacity of $12.8\,mAh\,cm^{-2}$ with moderative CE 98% and 88%, respectively, over 70 cycles (Figure 4C). At a lower current density of $0.47\,mA\,cm^{-2}$, the energy density and areal capacity further increased to $440\,Wh\,L^{-1}$ and $25\,mAh\,cm^{-2}$, respectively, with 10% capacity loss after 10 cycles or 500 h. A comparison of the areal capacity with those of other cathode materials is presented in Figure 4A.[33–38]

The volumetric energy density versus areal sulfur-loading plot shows that the slimmed-down pC@CN-CNT cell is superior to most of the high-energy-density LSB cells recently reported, where the Li metal anode is still in 60% excess of the stoichiometric amount[36,39–49] (Figure 4D). In addition, the energy stored in the cell (~40 mWh) is compelling, as it is about 6.7 times higher than that (~6 mWh) of the cell with a volumetric energy density of $550\,Wh\,L^{-1}$ (Figure 4E).[48] The cells in Reference [45] were excluded from the consideration, as the dimensions of the cell components are not specified; however, the energy stored was roughly estimated by assuming a unit electrode area of $1\,cm^2$. One might realize that prior research efforts were, so far, geared toward the upper left side of the volumetric energy density versus areal sulfur-loading plot. This means that a high volumetric energy density is mainly achieved by utilizing thin ($<50\,\mu m$) sulfur electrodes under high sulfur-loading conditions ($<10\,mg_S\,cm^{-2}$) with superior electron/ion transfer and less passivation on both the anode and cathode. The benefits of the thin electrode strategy are often canceled out by electrode stacking or rolling, which significantly accelerates the typical issues

and thereby results in more rapid cell failure than expected.[50] This is why laboratory-scale LSB coin cell tests are hardly adaptable to practical cells. Such difficulties are minimal and, at least, partly mitigated by utilizing the thick electrode with ultrahigh sulfur loading in the pC@CN-based LSB cells. To take one step closer to practical application, we are currently working on fabricating centimeter-thick free-standing pC@CN electrodes that will be installed into 18,650 cells for electrochemical characterization.

# 4 | CONCLUSION

In conclusion, we demonstrated that large mesoporous microspheres of C@CN provide a facile and practical route for achieving high-areal-capacity and high-energy-density LSBs. The key to high performance is the synergy between the large mesopores and heptazine-based surface functional groups on C@CN, which efficiently promotes the lower plateau reactions and thereby enables high utilization of sulfur with only minor capacity loss under ultrahigh sulfur-loading conditions. These properties were retrofitted into high-loading sulfur cathodes by using precipitates prepared by molecular cooperative assembly between glucose and triazine molecules as precursors, which could be pressed into a pellet, yielding a free-standing electrode that exhibited a potential for scale-up. The electrode composition could also be controlled by tailoring the pore structure and N content. Combined with high-conductive current collectors such as CC or CNT buckypaper in series, the pC@CN electrode achieved an areal capacity of 24 and $17\,mAh\,cm^{-2}$ at 0.47 and $4.7\,mA\,cm^{-2}$, respectively (at $24\,mg_S\,cm^{-2}$), thereby meeting the requirements to compete with the state-of-the-art LIBs. After careful cell optimization, the pC@CN-based LSB cells afforded a total energy storage of 39 mWh, corresponding to a volumetric energy density of $440\,Wh\,L^{-1}$, while realizing high sulfur loading ($24\,mg_S\,cm^{-2}$), sulfur fraction (70%), utilization (61%), and electrode thickness ($20.8\,\mu m$ per $1\,mg_S\,cm^{-2}$) with excess lithium metal anode (60%).

## CONFLICT OF INTERESTS

The authors declare that there are no conflict of interests. [Correction added on 28 July 2021, after first online publication: Conflict of Interest section has been added.]

## ORCID

*Hui-Ju Kang* https://orcid.org/0000-0003-2735-1161
*Tae-Gyu Lee* https://orcid.org/0000-0002-7041-2356
*Heejin Kim* https://orcid.org/0000-0003-3027-6983
*Jae-Woo Park* https://orcid.org/0000-0002-7916-6809
*Hyun Jin Hwang* https://orcid.org/0000-0001-7163-018X
*Kwang-Suk Jang* https://orcid.org/0000-0001-5835-9364
*Hae Jin Kim* https://orcid.org/0000-0002-1960-0650
*Yun Suk Huh* https://orcid.org/0000-0003-1612-4473
*Won Bin Im* https://orcid.org/0000-0003-2473-4714
*Young-Si Jun* https://orcid.org/0000-0002-7157-4920

## REFERENCES

1. Divya KC, Ostergaard J. Battery energy storage technology for power systems—an overview. *Electr Power Syst Res*. 2009;79: 511-520.
2. Hagen M, Hanselmann D, Ahlbrecht K, Maca R, Gerber D, Tubke J. Lithium–sulfur cells: the gap between the state-of-the-art and the requirements for high energy battery cells. *Adv Energy Mater*. 2015;5:1401986.
3. Goldie-Scot L. *A Behind the Scenes Take on Lithium-ion Battery Prices*. San Francisco, CA: BloombergNEF; 2019.
4. Ji XL, Evers S, Black R, Nazar LF. Stabilizing lithium–sulphur cathodes using polysulphide reservoirs. *Nat Commun*. 2011;2: 325.
5. Mikhaylik YV, Akridge JR. Polysulfide shuttle study in the Li/S battery system. *J Electrochem Soc*. 2004;151:A1969-A1976.
6. Kim KH, Jun Y-S, Gerbec JA, See KA, Stucky GD, Jung H-T. Sulfur infiltrated mesoporous graphene–silica composite as a polysulfide retaining cathode material for lithium–sulfur batteries. *Carbon*. 2014;69:543-551.
7. Ji X, Lee KT, Nazar LF. A highly ordered nanostructured carbon–sulphur cathode for lithium–sulphur batteries. *Nat Mater*. 2009:500-506.
8. Chung S-H, Chang C-H, Manthiram A. Progress on the critical parameters for lithium–sulfur batteries to be practically viable. *Adv Funct Mater*. 2018;28:1801188.
9. Emerce NB, Eroglu D. Effect of electrolyte-to-sulfur ratio in the cell on the Li–S battery performance. *J Electrochem Soc*. 2019;166:A1490-A1500.
10. Wu XW, Xie H, Deng Q, et al. Three-dimensional carbon nanotubes forest/carbon cloth as an efficient electrode for lithium–polysulfide batteries. *ACS Appl Mater Interfaces*. 2017;9:1553-1561.
11. Chung S-H, Chang C-H, Manthiram A. Hierarchical sulfur electrodes as a testing platform for understanding the high-loading capability of Li–S batteries. *J Power Sources*. 2016;334: 179-190.
12. Schuster J, He G, Mandlmeier B, et al. Spherical ordered mesoporous carbon nanoparticles with high porosity for lithium–sulfur batteries. *Angew Chem Int Ed*. 2012;51: 3591-3595.
13. Balach J, Jaumann T, Klose M, Oswald S, Eckert J, Giebeler L. Mesoporous carbon interlayers with tailored pore volume as polysulfide reservoir for high-energy lithium–sulfur batteries. *J Phys Chem C*. 2015;119:4580-4587.
14. Xu F, Tang Z, Huang S, et al. Facile synthesis of ultrahigh-surface-area hollow carbon nanospheres for enhanced adsorption and energy storage. *Nat Commun*. 2015;6:7221.
15. Li D, Han F, Wang S, Cheng F, Sun Q, Li W-C. High sulfur loading cathodes fabricated using peapodlike, large pore volume mesoporous carbon for lithium–sulfur battery. *ACS Appl Mater Interface*. 2013;5:2208-2213.
16. Manthiram A, Fu Y, Chung S-H, Zu C, Su Y-S. Rechargeable lithium–sulfur batteries. *Chem Rev*. 2014;114: 11751-11787.
17. Imtiaz S, Zhang J, Zafar ZA, et al. Biomass-derived nanostructured porous carbons for lithium–sulfur batteries. *Sci China Mater*. 2016;59:389-407.
18. Jun Y-S, Lee EZ, Wang X, Hong WH, Stucky GD, Thomas A. From melamine-cyanuric acid supramolecular aggregates to carbon nitride hollow spheres. *Adv Funct Mater*. 2013;23: 3661-3667.
19. Kang H-J, Huh YS, Im WB, Jun Y-S. Molecular cooperative assembly-mediated synthesis of ultra-high-performance hard carbon anodes for dual-carbon sodium hybrid capacitors. *ACS Nano*. 2019;13:11935-11946.
20. Zinin PV, Ming L-C, Sharma SK, et al. Ultraviolet and near-infrared Raman spectroscopy of graphitic $C_3N_4$ phase. *Chem Phys Lett*. 2009;472:69-73.
21. Lau VW, Moudrakovski I, Botari T, et al. Rational design of carbon nitride photocatalysts by identification of cyanamide defects as catalytically relevant sites. *Nat Commun*. 2016;7: 12165.
22. Ferrari A, Robertson J, Reich S, Thomsen C. Raman spectroscopy of graphite. *Philos Trans Royal Soc A*. 2004;362: 2271-2288.
23. Song J-Y, Lee H-H, Hong W, et al. A polysulfide-infiltrated carbon cloth cathode for high-performance flexible lithium–sulfur batteries. *Nanomaterials*. 2018;8:90.
24. Chung SH, Chang CH, Manthiram A. A carbon-cotton cathode with ultrahigh-loading capability for statically and dynamically stable lithium–sulfur batteries. *ACS Nano*. 2016;10: 10462-10470.
25. Zhang Q, Wang Y, Seh ZW, Fu Z, Zhang R, Cui Y. Understanding the anchoring effect of two-dimensional layered materials for lithium–sulfur batteries. *Nano Lett*. 2015;15: 3780-3786.
26. Jeong T-G, Choi DS, Song H, et al. Heterogeneous catalysis for lithium–sulfur batteries: enhanced rate performance by promoting polysulfide fragmentations. *ACS Energy Lett*. 2017;2: 327-333.
27. Deng Z, Zhang Z, Lai Y, Liu J, Li J, Liu Y. Electrochemical impedance spectroscopy study of a lithium/sulfur battery: modeling and analysis of capacity fading. *J Electrochem Soc*. 2013;160:A553-A558.
28. Li A, Liu H-L, Wang H, et al. Effects of temperature and heating rate on the characteristics of molded bio-char. *BioResources*. 2016;11:3259-3274.

29. Danner T, Singh M, Hein S, Kaiser J, Hahn H, Latz A. Thick electrodes for Li-ion batteries: a model-based analysis. *J Power Sources*. 2016;334:191-201.

30. Abe H, Kubota M, Nemoto M, et al. High-capacity thick cathode with a porous aluminum current collector for lithium secondary batteries. *J Power Sources*. 2016;334:78-85.

31. Singh M, Kaiser J, Hahn H. Thick electrodes for high energy lithium ion batteries. *J Electrochem Soc*. 2015;162: A1196-A1201.

32. Li Z, Yuan L, Yi Z, et al. Insight into the electrode mechanism in lithium–sulfur batteries with ordered microporous carbon confined sulfur as the cathode. *Adv Energy Mater*. 2014;4:1301473.

33. Luo L, Manthiram A. Rational design of high-loading sulfur cathodes with a poached-egg-shaped architecture for long-cycle lithium–sulfur batteries. *ACS Energy Lett*. 2017;2: 2205-2211.

34. Chang C-H, Chung S-H, Manthiram A. Highly flexible, free-standing tandem sulfur cathodes for foldable Li-S batteries with a high areal capacity. *Mater Horiz*. 2017;4:249-258.

35. Hong X, Jin J, Wu T, et al. A rGO–CNT aerogel covalently bonded with a nitrogen-rich polymer as a polysulfide adsorptive cathode for high sulfur loading lithium–sulfur batteries. *J Mater Chem A*. 2017;5:14775-14782.

36. Qie L, Zu CX, Manthiram A. A high-energy lithium–sulfur battery with ultrahigh-loading lithium polysulfide cathode and its failure mechanism. *Adv Energy Mater*. 2016;6:1502459.

37. Fang R, Zhao S, Hou P, et al. 3D interconnected electrode materials with ultrahigh areal sulfur loading for Li-S batteries. *Adv Mater*. 2016;28:3374-3382.

38. Chung S-H, Chang C-H, Manthiram A. A core–shell electrode for dynamically and statically stable Li-S battery chemistry. *Energy Environ Sci*. 2016;9:3188-3200.

39. Xue W, Miao L, Qie L, et al. Gravimetric and volumetric energy densities of lithium–sulfur batteries. *Curr Opin Electrochem*. 2017;6:92-99.

40. Kang H-S, Sun Y-K. Freestanding bilayer carbon–sulfur cathode with function of entrapping polysulfide for high performance Li-S batteries. *Adv Funct Mater*. 2016;26:1225-1232.

41. Zhou G, Li L, Ma C, et al. A graphene foam electrode with high sulfur loading for flexible and high energy Li-S batteries. *Nano Energy*. 2015;11:356-365.

42. Zhou G, Zhao Y, Manthiram A. Dual-confined flexible sulfur cathodes encapsulated in nitrogen-doped double-shelled hollow carbon spheres and wrapped with graphene for Li-S batteries. *Adv Energy Mater*. 2015;5:1402263.

43. Chung S-H, Chang C-H, Manthiram A. Robust, ultra-tough flexible cathodes for high-energy Li-S batteries. *Small*. 2016; 12:939-950.

44. Cheng X-B, Peng H-J, Huang J-Q, et al. Three-dimensional aluminum foam/carbon nanotube scaffolds as long- and short-range electron pathways with improved sulfur loading for high energy density lithium–sulfur batteries. *J Power Sources*. 2014;261:264-270.

45. Zhou W, Guo B, Gao H, Goodenough JB. Low-cost higher loading of a sulfur cathode. *Adv Energy Mater*. 2016;6:1502059.

46. Li Z, Zhang JT, Chen YM, Li J, Lou XW. Pie-like electrode design for high-energy-density lithium–sulfur batteries. *Nat Commun*. 2015;6:8850.

47. Yuan Z, Peng HJ, Huang JQ, et al. Hierarchical free-standing carbon-nanotube paper electrodes with ultrahigh sulfur-loading for lithium–sulfur batteries. *Adv Funct Mater*. 2014;24: 6105-6112.

48. Kim JH, Lee YH, Cho SJ, et al. Nanomat Li-S batteries based on all-fibrous cathode/separator assemblies and reinforced Li metal anodes: towards ultrahigh energy density and flexibility. *Energy Environ Sci*. 2019;12:177-186.

49. Mao Y, Li G, Guo Y, et al. Foldable interpenetrated metal-organic frameworks/carbon nanotubes thin film for lithium–sulfur batteries. *Nat Commun*. 2017;8:14628.

50. Salihoglu O, Demir-Cakan R. Factors affecting the proper functioning of a 3Ah Li-S pouch cell. *J Electrochem Soc*. 2017; 164:A2948-A2955.

## SUPPORTING INFORMATION

Additional Supporting Information may be found online in the supporting information tab for this article.